

The H I mass function in the Parkes H I Zone of Avoidance survey

Khaled Said^{1*†}, Renée C. Kraan-Korteweg², Lister Staveley-Smith^{3,4}

¹Research School of Astronomy and Astrophysics, Australian National University, Canberra, ACT 2611, Australia

²Astronomy Department, University of Cape Town, Private Bag X3, Rondebosch, 7701, South Africa

³International Centre for Radio Astronomy Research (ICRAR), M468, The University of Western Australia, 35 Stirling Highway, Crawley, WA 6009, Australia

⁴ARC Centre of Excellence for All Sky Astrophysics in 3 Dimensions (ASTRO 3D)

Accepted 2019 April 01. Received 2019 February 05; in original form 2018 September 05

ABSTRACT

An H I mass function (HIMF) was derived for 751 galaxies selected from the deep Parkes H I survey across the Zone of Avoidance (HIZOA). HIZOA contains both the Great Attractor Wall and the Local Void, two of the most extreme environments in the local Universe, making the sample eminently suitable to explore the overall HIMF as well as its dependence on local environment. To avoid any selection bias because of the different distances of these large-scale structures, we first used the two-dimensional stepwise maximum-likelihood method for the definition of an average HIMF. The resulting parameters of a Schechter-type HIMF for the whole sample are $\alpha = -1.33 \pm 0.05$, $\log(M_{\text{HI}}^*/M_{\odot}) = 9.93 \pm 0.04$, and $\phi^* = (3.9 \pm 0.6) \times 10^{-3} \text{ Mpc}^{-3}$. We then used the k -th nearest-neighbour method to subdivide the sample into four environments of decreasing local density and derived the Schechter parameters for each subsample. A strong trend is observed, for the slope α of the low-mass end of the HIMF. The slope changes from being nearly flat, i.e. $\alpha = -0.99 \pm 0.19$ for galaxies residing in the densest bin, to the steep value of $\alpha = -1.31 \pm 0.10$ in the lowest density bin. The characteristic mass, however, does not show a clear trend between the highest and lowest density bins. We find similar trends in the low-mass slope when we compare the results for a region dominated by the Great Attractor, and the Local Void, which are found to be over-, respectively underdense by 1.35 and 0.59 compared to the whole sample.

Key words: galaxies: distances and redshifts – galaxies: mass function – cosmology: observations – cosmology: large-scale structure of Universe

1 INTRODUCTION

The H I mass function (HIMF) is the number of galaxies of a given H I mass in a given volume. The HIMF of galaxies is a key observational component to understand cosmology, large-scale structures of the Universe, and galaxy formation and evolution. It contains important information about the physical processes that add and remove the H I mass from galaxies, including ram pressure (Gunn & Gott 1972), thermal evaporation (Cowie & Songaila 1977), tidal forces (Shostak et al. 1984), and gravitational potential (Bekki 1999).

These physical processes usually proceed at different rates in different environments due to the dependence of interactions between galaxies as a function of the local galaxy density. As such, we do not expect that HIMF to be universal but that the shape will change from one environment to the other.

According to the galaxy evolution theory, a number of physical processes occur at a higher rate in high-density environments compared to low-density environments. One of these processes

is the tidal stripping which removes the H I gas from the interacting galaxies (Shostak et al. 1984). Another process that is directly proportional to the environmental density is the ram pressure. It was shown in two sequential papers (Gott & Gunn 1971; Gunn & Gott 1972) that the hot gas observed in X-rays in the Coma cluster (Meekins et al. 1971) is responsible for the stripping of gas from galaxies within the cluster due to ram pressure. Although tidal and collision stripping are more efficient in groups of galaxies, ram pressure is more efficient in clusters (English et al. 2010; Westmeier et al. 2013).

A direct way of observing the process of H I gas removal from galaxies in high-density regions is through dedicated high resolution H I surveys (e.g., Chung et al. 2009; Serra et al. 2012, 2013). Important clues can also be learned from the hydrodynamical simulations (e.g., Bekki et al. 2005). Such processes can also be detected statistically via constructing the HIMF across different environments ranging from low-density to high-density regions (e.g., Verheijen et al. 2001; Rosenberg & Schneider 2002; Springob et al. 2005; Zwaan et al. 2005; Pisano et al. 2011; Moorman et al. 2014; Jones et al. 2016; Westmeier et al. 2017; Jones et al. 2018).

Quantitative findings from the latter methods have been a de-

* E-mail: khaled.said@anu.edu.au

† IAU and Gruber Foundation Fellow

bated topic for over a decade. Verheijen et al. (2001) performed a VLA blind H I survey of the Ursa Major cluster with the aim to measure the slope of the HIMF down to low masses. They measured a flat slope for this region. Rosenberg & Schneider (2002) used the Arecibo Dual-Beam Survey to construct the HIMF for the entire sample and for 38 galaxies within the center of Virgo Cluster. They concluded that, the HIMF is less steep in high-density regions. The main limitation for these studies was the small number of galaxies in the low mass bins.

In 2005, two independent studies used larger number of galaxies to find contradicting conclusions. Springob et al. (2005) divides their H I galaxy sample into three subsets according to the local density reconstructed via the PSCz survey (Branchini et al. 1999). They found a steeper HIMF slope in the lowest density sample compared to the other two samples. Zwaan et al. (2005), on the other hand, used the k -th nearest neighbour metric (Dressler 1980) to divide their sample into five sub-samples according to their local density. They found that the low-mass slope of the HIMF depends only weakly on the local density, being steeper in higher density environments. They found no dependence of the characteristic H I-mass M^* on the local density.

More recent studies show that this tension holds even within the same survey. Moorman et al. (2014) and Jones et al. (2016) used 40% and 70% of the ALFALFA survey (Giovannelli et al. 2005), respectively, and found no significant dependence of the low-mass slope on the local density but a larger characteristic H I-mass M^* in high-density regions compared with low-density regions. Jones et al. (2018) later used the complete ALFALFA sample and found larger change in the low-mass slope than previously, in the sense that the low-mass slope is steeper in the high-density environments (not clusters) than in the low-density environment.

In this work, we take advantage of a blind H I survey that is more than twice as sensitive as HIPASS (Meyer et al. 2004; Koribalski et al. 2004) to construct a new HIMF. In addition, we probe the HIMF in different environments because this survey covers the most two extreme environment in terms of density in the local Universe, namely the Great Attractor (GA; Lynden-Bell et al. 1988; Woudt et al. 1999) and the Local Void (LV; Tully & Fisher 1987; Kraan-Korteweg et al. 2008).

This paper is organized as follows: The sample is presented in Section 2. In Section 3, we describe the methodology used to derive the HIMF. The universality of the HIMF is discussed in Section 4. Lastly, we summarize our results in Section 5. Throughout this paper, we used the Hubble constant of $H_0 = 75 \text{ km s}^{-1} \text{ Mpc}^{-1}$.

2 HIZOA SAMPLE

This study is based on the deep “blind” H I Zone of Avoidance survey (HIZOA) performed with the multibeam receiver of the 64 m Parkes radio telescope. This survey covers the inner Milky Way, $|b| < 5^\circ$, for the Galactic longitude range accessible from Parkes, $196^\circ < \ell < 52^\circ$. It includes both the southern ZOA (Staveley-Smith et al. 2016) and its extension to the north (Donley et al. 2005). It was originally designed to unveil the large-scale structures hidden behind the Milky Way. Significant parts of dynamically influential large-scale structures in the local Universe remained obscured from our view due to dust absorption and stellar crowding. This includes the Great Attractor region, considered to be an extreme overdensity in the nearby Universe (Lynden-Bell et al. 1988; Woudt et al. 1999), and the Local Void, which is the largest nearby void (Tully & Fisher 1987;

Kraan-Korteweg et al. 2008) and has been mapped particularly poorly due to its centre being located behind the Galactic Bulge. Further notable structures are the Puppis and Ophiuchus clusters (see Staveley-Smith et al. 2016, for details).

Given the dust obscuration and stellar confusion problems, systematic H I surveys are the only method to chart these structures (Staveley-Smith et al. 2016) and to quantitatively assess the extent of overdensities and underdensities. The survey achieved an rms sensitivity of 6 mJy in the velocity range of $v < 12000 \text{ km s}^{-1}$. Galaxies were detected within the range of $\log M_{\text{HI}}/M_\odot$ of 6.5 – 11.0 and, most importantly, the survey was sensitive to galaxies well below the characteristic H I-mass M_{HI}^* at the distance of the Great Attractor.

The primary goal of this paper is therefore to derive an average HIMF from HIZOA, and to explore the variation in the HIMF in some of the most extreme environments in the nearby Universe. The results will also improve our knowledge of the over/underdensities of regions obscured by the ZOA. These mass density estimates will be crucial in improving our understanding of the observed cosmic flow fields in the ZOA (e.g., Erdoğdu et al. 2006; Lavaux & Hudson 2011; Kraan-Korteweg et al. 2017; Sorce et al. 2017).

3 DERIVATION OF THE HIZOA H I MASS FUNCTION

We derive the H I mass function for all galaxies in the HIZOA survey that meet our selection criteria. The HIZOA survey has been characterized by three completeness limits: (1) velocity-integrated flux, (2) mean flux density, and (3) a hybrid limit (see Table 4 in Staveley-Smith et al. 2016). Above these limits lie between 70 per cent and 90 per cent of the HIZOA sample. These limits were derived using a modified version of the V/V_{max} test (Rauzy 2001) which, unlike the traditional V/V_{max} test (Schmidt 1968), is insensitive to the presence of large-scale structure. For the current study, we use the hybrid limit, which has the sharpest cutoff and therefore most likely to represent the true HIZOA completeness limit.

The maximum volume to which a HIZOA galaxy can be detected (ignoring the profile resolution correction) with certainty is therefore

$$V_{\text{max}} = \frac{4\pi f_{\text{sky}}}{3} \left(\frac{M_{\text{HI}}}{8.815 \times 10^5 S_{\text{lim}} W_{50}^{0.74}} \right)^{3/2}, \quad (1)$$

where $S_{\text{lim}} = 18 \text{ mJy}$ represents the corresponding $T = -2$ completeness limit (Staveley-Smith et al. 2016), W_{50} is the velocity width (in km s^{-1}), f_{sky} is the fraction of the sky covered by the survey, and M_{HI} is given by

$$M_{\text{HI}} = 2.356 \times 10^5 D^2 F_{\text{HI}} M_\odot, \quad (2)$$

where D is the distance in Mpc and F_{HI} is the flux integral. We can then fit a Schechter function (Schechter 1976) to the binned density estimates of the form:

$$\Phi(M_{\text{HI}}) = \ln 10 \phi^* \left(\frac{M_{\text{HI}}}{M_*} \right)^{\alpha+1} e^{-\frac{M_{\text{HI}}}{M_*}}, \quad (3)$$

to the derived H I mass function.

However, as with the V/V_{max} test, a major problem of the $1/V_{\text{max}}$ method for deriving the H I mass function is sensitivity to large-scale structure, such that the measured mass function does not represent the universal H I mass function. For sub-samples where it can be assumed that the HIMF has a similar shape, but different normalisation, the two-dimensional stepwise maximum likelihood

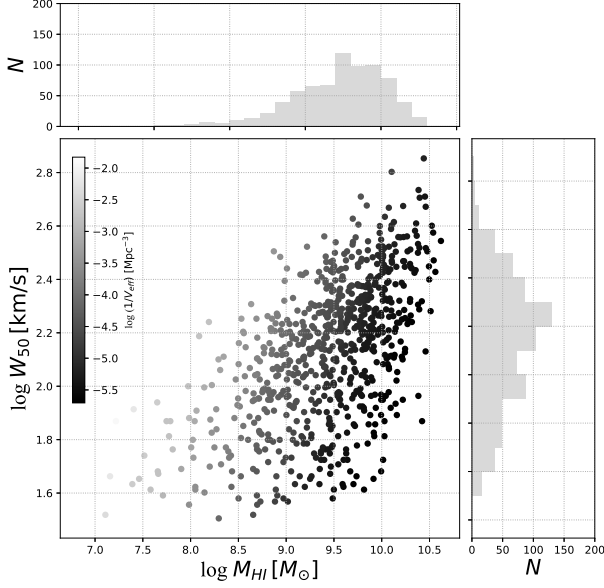


Figure 1. The galaxy density distribution in the $M_{\text{HI}} - W_{50}$ plane. The gray scale represents the reciprocal of the effective volume for each galaxy in which it can be found. This effective volume is calculated via the two-dimensional stepwise maximum likelihood method.

method (2DSWML: Loveday 2000; Zwaan et al. 2003, 2005) can be deployed.

The 2DSWML method finds the maximum likelihood solutions for the number density of galaxies ϕ_{jk} as a function of HI mass and velocity width by iterating from an initial guess:

$$\phi_{jk} = \frac{\sum_{i=1}^{N_g} \delta(M_i - M_j, W_i - W_k)}{\sum_{i=1}^{N_g} \frac{H_{ijk} \Delta M \Delta W}{\sum_{l=1}^{N_M} \sum_{m=1}^{N_W} \phi_{ilm} H_{ilm} \Delta M \Delta W}}, \quad (4)$$

where δ_{ijk} is a function equals one if a galaxy i belongs to the HI mass bin j and velocity width bin k , and equals zero otherwise. The function H_{ijk} equals the fraction available of the bin jk in which a galaxy i resides (Zwaan et al. 2003).

Equation 4 can be interpreted in different ways. The denominator for example, presents the effective volume available to galaxies in bin jk , and can be modified to find the effective volume available to each galaxy as in Zwaan et al. (2005). Marginalizing Eq. 4 over the velocity width W gives the HI mass function (Martin et al. 2010; Jones et al. 2016) while marginalizing over the HI mass M_{HI} gives the velocity width function (Papastergis et al. 2011).

We used Eq. 4 to evaluate the effective volume available to each single galaxy after applying the completeness function of the HIZOA survey. Figure 1 shows the galaxy density distribution in the $M_{\text{HI}} - W_{50}$ plane where the gray scale represents the reciprocal of the effective volume available to each galaxy. There is a strong correlation between the linewidth and the effective volume. The histogram of the linewidth on the right-hand side of the plot shows that our sample contains a fair distribution of large and small galaxies, following an approximately Gaussian distribution.

We then marginalized ϕ_{jk} over the velocity width to calculate

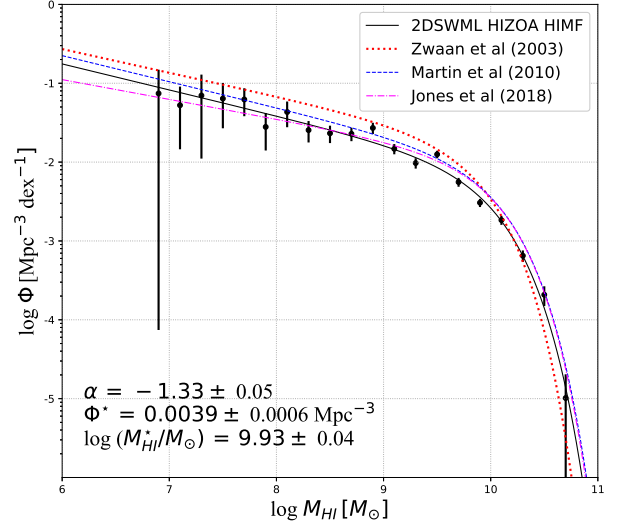


Figure 2. HIZOA HI mass function derived via the two-dimensional stepwise maximum likelihood method (Black-solid line). For comparison, the HI mass function of HIPASS BGC (dotted-red line; Zwaan et al. 2003), ALFALFA 40% (dashed-blue line; Martin et al. 2010), and ALFALFA 100% (dashed-dotted-fuchsia line; Jones et al. 2018) are also displayed.

the HIMF as:

$$\phi_j = \sum_{k=1}^{N_W} \phi_{jk} \Delta W \quad (5)$$

Figure 2 shows the result of this process for the whole sample above the completeness limit. The dots present the number space density in HI mass bins, the solid line is the best fit Schechter function of the form presented in Eq. 3, and the error bars are the Poisson errors. The final parameters of the HI mass function are:

- $\alpha = -1.33 \pm 0.05$
- $\log(M_{\text{HI}}^*/M_\odot) = 9.93 \pm 0.04$
- $\phi^* = (3.9 \pm 0.6) \times 10^{-3} \text{ Mpc}^{-3}$

For comparison, we add to Fig. 2 the Zwaan et al. (2003) results as a dotted line, Martin et al. (2010) as a dashed line, and Jones et al. (2018) as a dashed-dotted line. The faint-end slope derived here agrees, within the uncertainty, with Zwaan et al. (2003), Zwaan et al. (2005), Martin et al. (2010), and Jones et al. (2018). The knee of the HI mass function derived here agrees more with the Martin et al. (2010) and Jones et al. (2018) results than Zwaan et al. (2003) and Zwaan et al. (2005), perhaps because the HIZOA survey is more closely matched in sensitivity to ALFALFA than HIPASS (Staveley-Smith et al. 2016).

4 UNIVERSALITY OF THE HIMF

In this section, we will extend our analysis and use the HIZOA sample to test the universality of the HIMF, i.e. we will derive the Schechter function parameters (α and M_{HI}^*) across various environments of local densities, from extreme low-density to high-density regions. To accomplish this we divide the HIZOA galaxies into subsamples using two independent methods to infer different environ-

ments: (i) the Bayesian nearest neighbours (Ivezić et al. 2005) to determine the local density in which each galaxies resides; and (ii) extreme large-scale structures which, in the case of HIZOA, are the Great Attractor and the Local Void (Staveley-Smith et al. 2016).

4.1 Bayesian k -th nearest neighbours algorithm

Dressler (1980), showed that the density and the associated error can be estimated by using the distance to the k -th nearest neighbour, d_k as $\Sigma_k = K/\frac{4}{3}\pi d_k^3$, and $\sigma_{\Sigma_k} = \sqrt{K}/\frac{4}{3}\pi d_k^3$, respectively. Therefore, the fractional error decreases with k at the cost of decreasing the spatial resolution. Ivezić et al. (2005), proposed a Bayesian based version of the k -th nearest neighbour algorithm to decrease the fractional error without decreasing the spatial resolution. This is achieved by calculating distances to all k nearest neighbours, d_i , where $i = 1, 2, \dots, k$, instead of calculating the distance to only the k -th nearest neighbour, d_k , as,

$$\Sigma_k = \frac{C}{\sum_{i=1}^k d_i^3} \quad (6)$$

where the normalization C is calculated as,

$$C = \frac{k(k+1)}{2 \times \frac{4}{3}\pi}. \quad (7)$$

In case of a sparse sample, the above Bayesian method (Ivezić et al. 2005) is less biased compare to the classic k -th nearest neighbour method (Dressler 1980; for comparison, we apply this classic method in Appendix A). The next step in this analysis is to choose the number of neighbours. Casertano & Hut (1985) showed that the sixth neighbour is a good choice to reduce fluctuations and still retain locality. For that reason we calculate distances to all the six nearest neighbours.

Another fact that needs to be accounted for is that, for a flux-limited sample, galaxies will be more luminous and appear to be more isolated at larger distances. This implies that a value for Σ_6 which decreases with distance, even where there is no change in local density. This effect is clearly observed in the top-panel of Fig. 3. We corrected for this effect using flux and volume-limited samples derived from the $S^3 - SAX$ semi-analytic simulation. This process is described step-by-step in Appendix B. The corrected Σ_6 is shown in the bottom-panel of Fig. 3, and removes significant differences in the distance distribution of samples of different density. The bottom-panel of Fig. 3 also shows that our sample becomes very sparse at high-redshift, so we limit all our calculation to galaxies with $v_{hel} \leq 8000 \text{ km s}^{-1}$.

Figure 4 shows a histogram of the corrected sixth nearest neighbour density, Σ_6 . We divided the whole sample into four sub-samples and plot them on a colour scale from the least dense regions (solid-blue) to the most dense regions (dotted-dashed-red). For each of these sub-samples we derived the HIMF using the 2DSWML method. Figure 5 shows the four derived HIMFs ranging from the lowest-density region (top panel) to the highest-density region (bottom panel). For comparison, we use the same mass range of $\log M_{HI}/M_{\odot} = 8.0 - 10.5$ for the four sub-samples.

Table 1 presents the derived Schechter parameters for these four sub-samples ranging from the least dense region to the most dense region based on the Bayesian version of the k -th nearest neighbours algorithm. Although the number of galaxies at the low mass end of each sub-sample are small, we find a clear trend: the

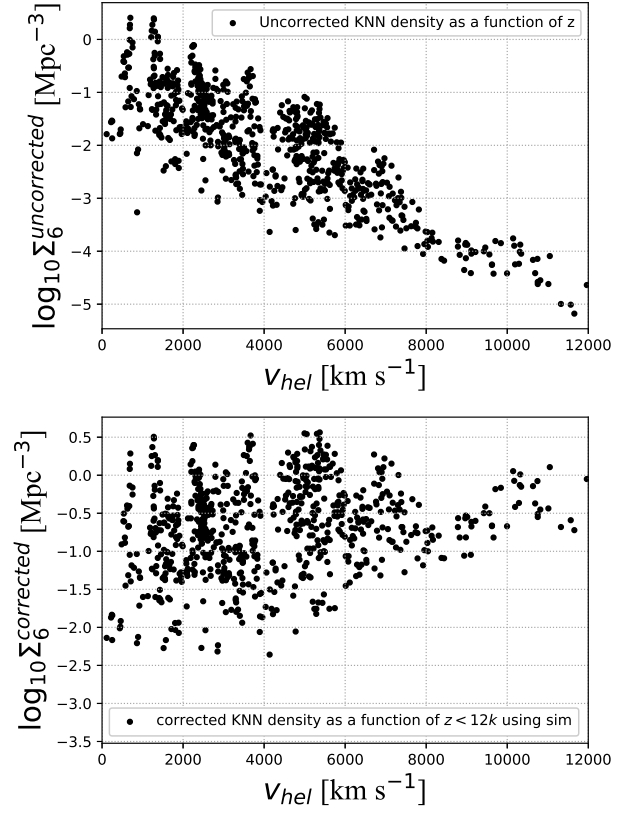


Figure 3. Scatter plot of the sixth nearest neighbour density, Σ_6 , using the Bayesian k nearest neighbours algorithm for HIZOA sample. The top-panel shows the uncorrected Σ_6 while the bottom-panel shows the corrected Σ_6 using the method presented in Appendix B

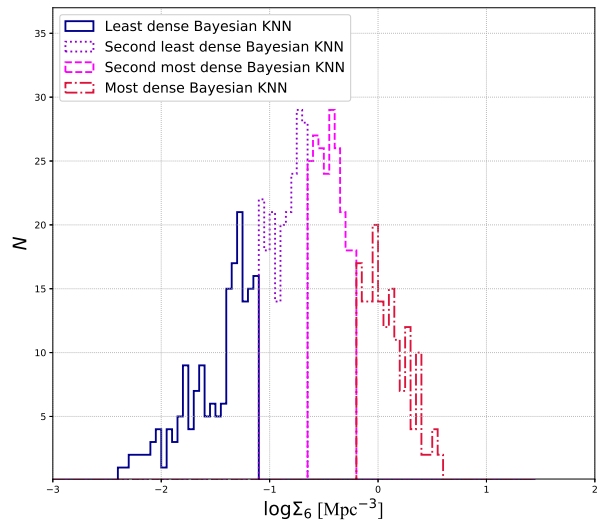


Figure 4. Histogram of the sixth nearest neighbour density, Σ_6 , using the Bayesian k nearest neighbours algorithm for the HIZOA galaxies divided into four groups according to Σ_6 .

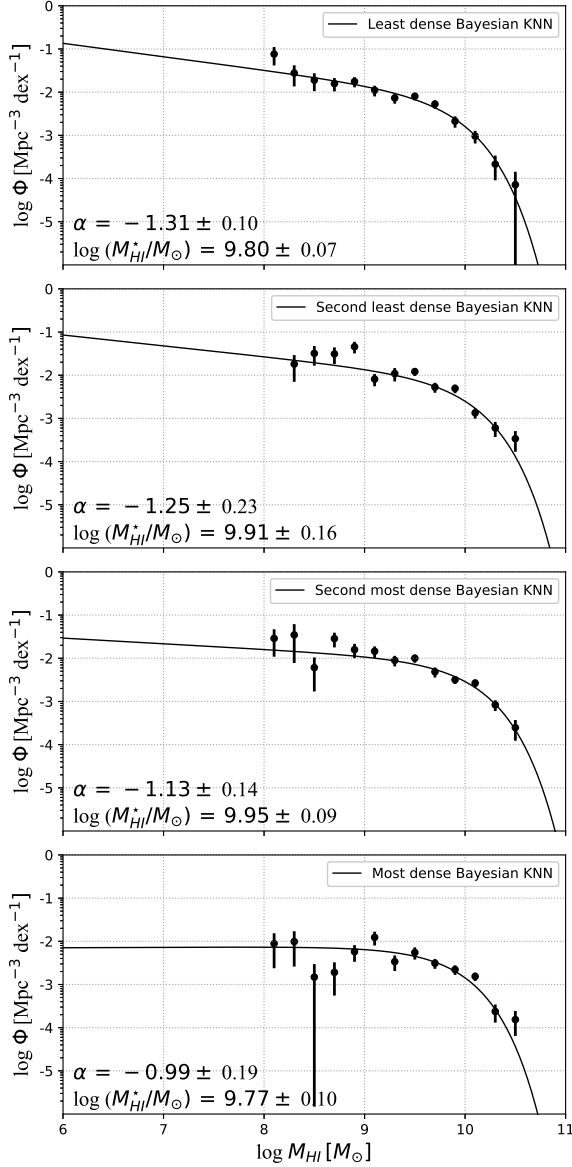


Figure 5. Four HIZOA HI mass function derived via the 2DSWML method based on the Bayesian density estimate. For comparison, the HIMFs are offset vertically to the normalization of the whole sample HIMF in Fig. 2.

HIMF is more shallow in high-density regions than in low-density regions.

A projection of the derived Schechter parameters on the $\alpha - \log M_{\text{HI}}^*$ plane is shown in Fig. 6. Confidence ellipses are defined with $(\alpha, \log M_{\text{HI}}^*, \sigma_{\alpha}, \sigma_{\log M_{\text{HI}}^*}, \theta)$, where θ is the angle between the x -axis and the major axis of the ellipses, and is measured via the covariance matrix of the correlated parameters:

$$\tan(2\theta) = 2 \frac{\sigma_{\alpha \log M_{\text{HI}}^*}}{\sigma_{\alpha}^2 - \sigma_{\log M_{\text{HI}}^*}^2}. \quad (8)$$

For uncorrelated parameters $\theta = \sigma_{xy} = \sigma_{yx} = 0$. This is contrary to what is found in Fig. 6 which displays the 1σ and 3σ confidence contours (dark and light ellipses respectively) which shows the Schechter parameters to be strongly correlated. We therefore find the HIMF not to be universal in shape. The derived param-

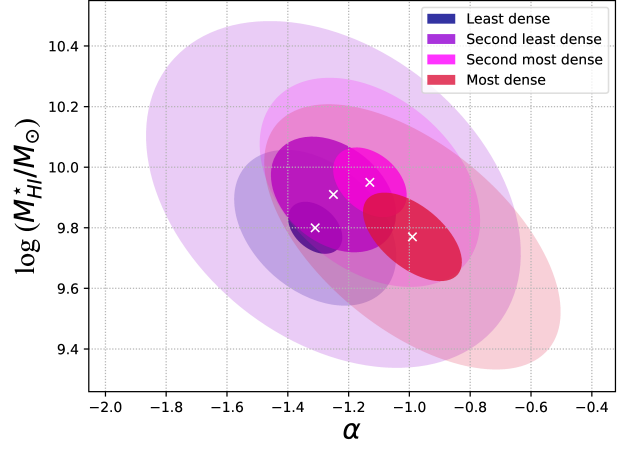


Figure 6. Schechter parameters for the four sub-samples divided according to their local density projected on the $\alpha - \log M_{\text{HI}}^*$ plane. Ellipses are defined with $(\alpha, \log M_{\text{HI}}^*, \sigma_{\alpha}, \sigma_{\log M_{\text{HI}}^*}, \theta)$ and plotted on a colour scale from the least dense regions (blue) to the most dense regions (red). Dark and light ellipses show 1σ and 3σ contours, respectively.

Table 1. Schechter parameters for the four sub-samples divided according to their local density derived by the Bayesian version of the k -th nearest neighbours algorithm.

Region	α	$\log(M_{\text{HI}}^*/M_{\odot})$
Least dense	-1.31 ± 0.10	9.80 ± 0.07
Second least dense	-1.25 ± 0.23	9.91 ± 0.16
Second most dense	-1.13 ± 0.14	9.95 ± 0.09
Most dense	-0.99 ± 0.19	9.77 ± 0.10

ters for the least dense environment and most dense environment deviate from each other. In particular, the slope α increases with density.

4.2 Known large-scale structures in ZOA

As previously mentioned, the HIZOA survey covers two of the most extreme galaxy structures in the Local Universe with the Great Attractor (GA) and the Local Void (LV). This provides us with two different laboratories of different density environment. We will derive the HIMF for each of these two structures.

The first structure in the HIZOA survey (Staveley-Smith et al. 2016) is the GA Wall crossing. This region dominates the HIZOA redshift survey and extends from $v_{\text{LG}} \sim 1500$ to ~ 7500 km s⁻¹ and from $l \sim 280^\circ$ to $\sim 330^\circ$. The second prominent structure, the LV extends from $l \sim 330^\circ$ to $\sim 45^\circ$ and spreads out over a volume to $v_{\text{LG}} \sim 6000$ km s⁻¹ (Tully & Fisher 1987; Donley et al. 2005; Kraan-Korteweg et al. 2008). The southern part of the LV lies within the main HIZOA survey (Staveley-Smith et al. 2016), whereas the northern part of is covered by the northern extension (Donley et al. 2005).

Figures 7 shows the HIMF derived from the LV (top-panel) and GA (bottom-panel) sub-samples, respectively, and Table 2 lists the derived Schechter parameters for the two regions. Again for comparison purposes, we use the same mass range of $\log M_{\text{HI}}/M_{\odot} = 8.0 - 10.5$ for the two sub-samples. There is a trend of increasing α when moving from the low-density region

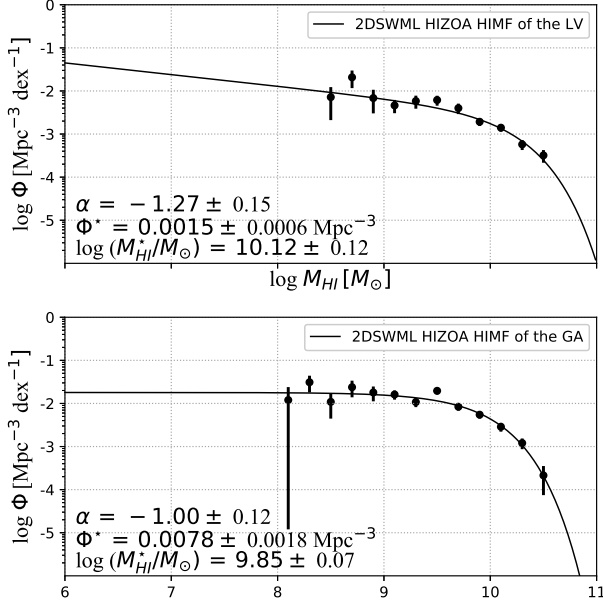


Figure 7. HIZOA HI mass function derived via the 2DSWML method for LV (top-panel) and GA (bottom-panel) regions.

Table 2. Schechter parameters for the LV and GA regions.

Region	α	$\log(M_{HI}^*/M_{\odot})$	ϕ^* (Mpc^{-3})
LV	-1.27 ± 0.15	10.12 ± 0.12	0.0015 ± 0.0006
GA	-1.00 ± 0.12	9.85 ± 0.07	0.0078 ± 0.0018

(LV) to high-density region (GA). This result is in **excellent** agreement with the analysis based on the Bayesian k -th nearest neighbours.

Confidence ellipses are shown on the $\alpha - \log M_{HI}^*$ plane for the GA and LV regions in Fig. 8. The derived Schechter parameters of the GA and LV regions do not agree within the 1σ errors, con-

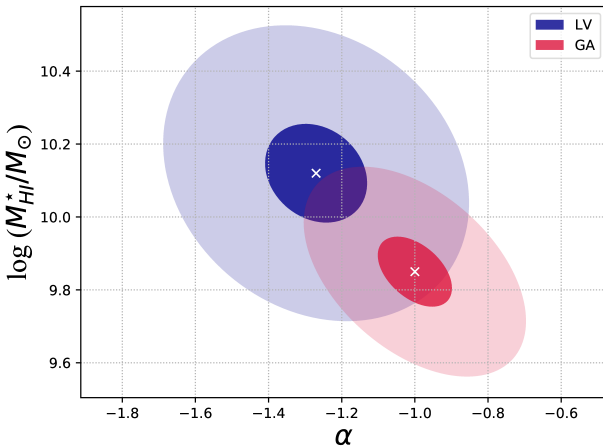


Figure 8. Schechter parameters for the GA and LV samples projected on the $\alpha - \log M_{HI}^*$ plane. Ellipses are defined as in Fig. 6

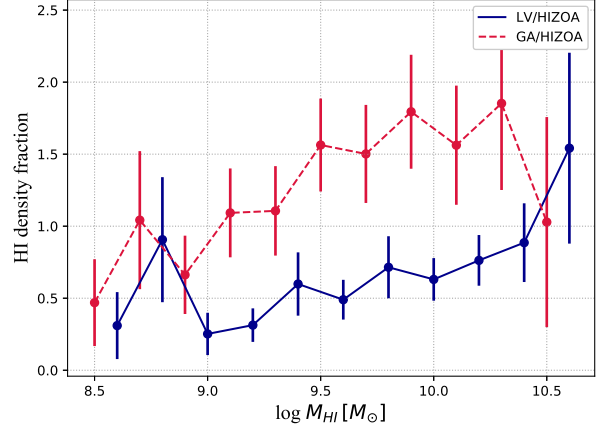


Figure 9. Density fraction of both the LV (blue) and GA (red) regions compared to the complete HIZOA sample. The error bars are the Poisson errors. The LV curve is shifted horizontally by 0.1 dex for clarity.

firming the previous results from the Bayesian k -th nearest neighbours.

We integrate the GA and LV HIMF over a mass range of $\log(M_{HI}^*/M_{\odot}) = 8.5 - 10.8$ and compare their values with full HIZOA HIMF integrated over the same mass range. This results in an overall overdensity in the GA region of 1.35 and underdensity in the LV region of 0.59 compared to the complete HIZOA sample.

Figure 9 displays a more nuanced comparison of the overdensity as a function of HI mass. In this Figure, we divide the derived LV and GA HIMF in Figure 8 by the HIZOA HIMF in Figure 2, resulting in the corresponding HI overdensities. This shows that low-density regions appear to contain similar densities of low-mass galaxies as high-density regions, implying that low-mass galaxies are either not formed in high-density regions or (more likely) responsible for the growth of high-mass galaxies through a merging and accretion process.

4.3 Discussion

Analysis of the HIZOA survey finds a steeper slope at the low HI-mass end of the HIMF in low-density regions compared to high-density regions. A simplified explanation of this result is that HI gas stripping processes act on small galaxies in high-density regions, and is likely the direct results of higher tidal, collisional, and ram pressure forces in these regions. Each of these processes is important, but their exact importance in different physical situations is not straightforward to predict and, furthermore, depends on physical quantities which are difficult to measure, such as IGM density.

The result agrees with Rosenberg & Schneider (2002) and Springob et al. (2005), who both found a similar trend of increasing α towards higher density regions. Verheijen et al. (2001) and Pisano et al. (2011) also found a shallow HIMF slope for Ursa Major and six groups similar to the Local Group, respectively compare to the field HIMF. Jones et al. (2016) and Moorman et al. (2014) used earlier versions of the ALFALFA catalogue (Giovannelli et al. 2005; Haynes et al. 2011) and found no significant change in the low-mass slope between high and low-density regions. On the other hand, Zwaan et al. (2005) and Jones et al. (2018) used the complete HIPASS and ALFALFA catalogs, respectively, and found that the

low-mass slope decreases towards high-density region. Their results are opposite to the trend derived from the HIZOA data set.

Table 3 presents a comparison of the derived HIMF parameters from a large number of different HI surveys that have been used to derive the HIMF. This comparison shows a tension between most of the results. It is possible in some cases that the selection of different nearest neighbour metrics could cause different scales and therefore different physical processes to be probed. However, we expect these discrepancies to be resolved in the near future with forthcoming deeper and more sensitive surveys such as the Wide-field ASKAP L-band Legacy All-sky Blind survey (WALLABY; Reynolds et al. 2019), the MeerKAT Fornax Survey (Serra et al. 2016), and the MeerKAT LADUMA survey (Blyth et al. 2016). The advantage of the WALLABY survey will be twofold: it will be less sensitive to cosmic variance due to the large volume; and it will push the detection to lower mass dwarf galaxies with $M_{\text{HI}} = 10^8 M_{\odot}$ out to distances of 60 Mpc (Koribalski 2012). The MeerKAT Fornax Survey will observe the Fornax cluster with high resolution to measure the HI low-mass slope down to $5 \times 10^5 M_{\odot}$, while the MeerKAT LADUMA survey (Blyth et al. 2016) will focus more on the evolution of the HI mass function since it will be able to measure the HI mass function out to higher redshifts.

5 SUMMARY

In this paper, we constructed the HI mass function for the Parkes HI Zone of Avoidance Survey using the two-dimensional step-wise maximum likelihood method. All galaxies in the HIZOA survey that meet our selection criteria ($N = 751$ galaxies) are included in the derivation of this HI mass function. The average parameters of the HI mass function are $\alpha = -1.33 \pm 0.05$, $\log(M_{\text{HI}}^*/M_{\odot}) = 9.93 \pm 0.04$, and $\phi^* = (3.9 \pm 0.6) \times 10^{-3} \text{ Mpc}^{-3}$. Comparisons of these parameters with values from the literature were made. We found that the faint-end slope derived here agrees, within the uncertainty, with HIPASS BGC, HICAT, ALFALFA 40%, and ALFALFA 100%. The characteristic mass derived here agrees better, however, with the ALFALFA HI mass function than with the HIPASS HI mass function. HIZOA is twice as sensitive as HIPASS, which means the depth of the survey is better matched with ALFALFA, though source confusion may be more common.

We took advantage of the mix of high and low-density environments covered by HIZOA to test the universality of the HI mass function. Two independent methods were used to define the local density environment for galaxies. The first method was the k -th nearest neighbour algorithm. In this method we used a Bayesian version to calculate distances to all the k nearest neighbours and not only the k -th nearest neighbour. This is more robust especially in the case of a sparse sample. The other method involved confining our analysis to two extreme environments located within the HIZOA survey area: the Local Void as a low-density environment and the Great Attractor as a high-density environment.

The above mentioned two methods lead to similar conclusion that: (i) the low-mass slope α , of the HI mass function is steeper in low-density environments than in high-density environments; and (ii) there is no clear trend of the characteristic HI mass M_{HI}^* with increasing density of the environment.

This conclusion align closely with theoretical predictions that the stripping of the HI mass occurs at higher rates in dense regions compared to low density regions due to the increase in the interaction rate of galaxies.

Comparison with other studies shows that not all previous results are in agreement. Forthcoming HI surveys with ASKAP, MeerKAT and the SKA will help resolve these issues and will be useful in understanding the details of the effect of environment on galaxy evolution.

ACKNOWLEDGMENTS

We acknowledge the HIZOA survey team for early access to the data. RCKK thanks the South African National Research Foundation for their support. Parts of this research were supported by the Australian Research Council Centre of Excellence for All Sky Astrophysics in 3 Dimensions (ASTRO 3D), through project number CE170100013.

REFERENCES

- Bekki K., 1999, *ApJ*, 510, L15
- Bekki K., Koribalski B. S., Ryder S. D., Couch W. J., 2005, *MNRAS*, 357, L21
- Blyth S. et al., 2016, in *Proceedings of MeerKAT Science: On the Pathway to the SKA*. 25-27 May, 2016 Stellenbosch, South Africa (MeerKAT2016). p. 4
- Branchini E. et al., 1999, *MNRAS*, 308, 1
- Casertano S., Hut P., 1985, *ApJ*, 298, 80
- Chung A., van Gorkom J. H., Kenney J. D. P., Crowl H., Vollmer B., 2009, *AJ*, 138, 1741
- Cowie L. L., Songaila A., 1977, *Nature*, 266, 501
- Donley J. L. et al., 2005, *AJ*, 129, 220
- Dressler A., 1980, *ApJ*, 236, 351
- English J., Koribalski B., Bland-Hawthorn J., Freeman K. C., McCain C. F., 2010, *AJ*, 139, 102
- Erdoğdu P. et al., 2006, *MNRAS*, 373, 45
- Giovanelli R. et al., 2005, *AJ*, 130, 2598
- Gott III J. R., Gunn J. E., 1971, *ApJ*, 169, L13
- Gunn J. E., Gott III J. R., 1972, *ApJ*, 176, 1
- Haynes M. P. et al., 2011, *AJ*, 142, 170
- Ivezić Ž., Vivas A. K., Lupton R. H., Zinn R., 2005, *AJ*, 129, 1096
- Jones M. G., Haynes M. P., Giovanelli R., Moorman C., 2018, *MNRAS*, 477, 2
- Jones M. G., Papastergis E., Haynes M. P., Giovanelli R., 2016, *MNRAS*, 457, 4393
- Koribalski B. S., 2012, *pasa*, 29, 359
- Koribalski B. S. et al., 2004, *AJ*, 128, 16
- Kraan-Korteweg R. C., Cluver M. E., Bilicki M., Jarrett T. H., Colless M., Elagali A., Böhringer H., Chon G., 2017, *MNRAS*, 466, L29
- Kraan-Korteweg R. C., Shafi N., Koribalski B. S., Staveley-Smith L., Buckland P., Henning P. A., Fairall A. P., 2008, *Outlining the Local Void with the Parkes HI ZOA and Galactic Bulge Surveys*. p. 13
- Lavaux G., Hudson M. J., 2011, *MNRAS*, 416, 2840
- Loveday J., 2000, *MNRAS*, 312, 557
- Lynden-Bell D., Faber S. M., Burstein D., Davies R. L., Dressler A., Terlevich R. J., Wegner G., 1988, *ApJ*, 326, 19
- Martin A. M., Papastergis E., Giovanelli R., Haynes M. P., Springob C. M., Stierwalt S., 2010, *ApJ*, 723, 1359
- Meekins J. F., Fritz G., Chubb T. A., Friedman H., 1971, *Nature*, 231, 107

Table 3. Comparison of the HIMF parameters derived from different surveys. 1. Zwaan et al. (1997), 2. Verheijen et al. (2001), 3. Rosenberg & Schneider (2002), 4. Zwaan et al. (2003), 5. Zwaan et al. (2005), 6. Springob et al. (2005), 7. Martin et al. (2010), 8. Jones et al. (2016), 9. Jones et al. (2018), 10. Westmeier et al. (2017), and 11. This work

Reference	Galaxies	Sky Area (deg ²)	rms (mJy)	Mass Range log(M_{HI}/M_{\odot})	α	M_{HI}^* M_{\odot}	ϕ^* Mpc ⁻³	Note on the environmental effects	Survey
(1)	66	65	0.75	7.0-10.0	-1.20	9.55	0.014	—	HI Strip (AHISS)
(2)	32	—	0.79	7.0-10.0	—	9.8	0.08	$\rho \uparrow \Rightarrow \alpha \uparrow$	VLA Ursa Major
(3)	265	430	3.5	7.0-10.0	-1.53	9.88	0.005	$\rho \uparrow \Rightarrow \alpha \uparrow$	Dual-Beam (ADBS)
(4)	1000	20626	13	6.8-10.6	-1.30	9.79	0.009	—	HIPASS (BGC)
(5)	4315	21346	13	6.8-10.6	-1.37	9.80	0.006	$\rho \uparrow \Rightarrow \alpha \downarrow$	HIPASS (HICAT)
(6)	2771	10602	—	7.0-10.0	-1.24	9.99	0.003	$\rho \uparrow \Rightarrow \alpha \uparrow$ and $M_{HI}^* \downarrow$	Optically selected sample
(7)	10119	2607	2.4	6.2-11.0	-1.33	9.96	0.005	—	ALFALFA 40%
(8)	20000	4830	2.4	6.2-11.0	—	—	—	$\rho \uparrow \Rightarrow M_{HI}^* \uparrow$	ALFALFA 70%
(9)	—	6900	2.4	6.2-11.0	-1.25	9.94	0.005	$\rho \uparrow \Rightarrow \alpha \downarrow$ and $M_{HI}^* \uparrow$	ALFALFA 100%
(10)	31	—	4.0	6.6-9.4	-1.10	—	—	$\rho \uparrow \Rightarrow \alpha \uparrow$	Parkes Sculptor group
(11)	751	1230	6	7.0-10.6	-1.33	9.93	0.004	$\rho \uparrow \Rightarrow \alpha \uparrow$	HIZOA

Meyer M. J. et al., 2004, MNRAS , 350, 1195
 Moorman C. M., Vogeley M. S., Hoyle F., Pan D. C., Haynes M. P., Giovanelli R., 2014, MNRAS , 444, 3559
 Obreschkow D., Klöckner H.-R., Heywood I., Levrier F., Rawlings S., 2009, ApJ , 703, 1890
 Papastergis E., Martin A. M., Giovanelli R., Haynes M. P., 2011, ApJ , 739, 38
 Pisano D. J., Barnes D. G., Staveley-Smith L., Gibson B. K., Kilborn V. A., Freeman K. C., 2011, ApJS , 197, 28
 Rauzy S., 2001, MNRAS , 324, 51
 Reynolds T. N. et al., 2019, MNRAS , 482, 3591
 Rosenberg J. L., Schneider S. E., 2002, ApJ , 567, 247
 Schechter P., 1976, ApJ , 203, 297
 Schmidt M., 1968, ApJ , 151, 393
 Serra P. et al., 2016, in Proceedings of MeerKAT Science: On the Pathway to the SKA. 25-27 May, 2016 Stellenbosch, South Africa (MeerKAT2016). p. 8
 Serra P. et al., 2013, MNRAS , 428, 370
 Serra P. et al., 2012, MNRAS , 422, 1835
 Shostak G. S., Sullivan III W. T., Allen R. J., 1984, A&A, 139, 15
 Sorce J. G., Colless M., Kraan-Korteweg R. C., Gottlöber S., 2017, MNRAS , 471, 3087
 Springel V. et al., 2005, Nature , 435, 629
 Springob C. M., Haynes M. P., Giovanelli R., 2005, ApJ , 621, 215
 Staveley-Smith L., Kraan-Korteweg R. C., Schröder A. C., Henning P. A., Koribalski B. S., Stewart I. M., Heald G., 2016, AJ , 151, 52
 Tully R. B., Fisher J. R., 1987, Atlas of Nearby Galaxies
 Verheijen M. A. W., Trentham N., Tully B., Zwaan M., 2001, in Hibbard J. E., Rupen M., van Gorkom J. H., eds, Astronomical Society of the Pacific Conference Series Vol. 240, Gas and Galaxy Evolution. p. 507
 Westmeier T., Koribalski B. S., Braun R., 2013, MNRAS , 434, 3511
 Westmeier T. et al., 2017, MNRAS , 472, 4832
 Woudt P. A., Kraan-Korteweg R. C., Fairall A. P., 1999, A&A, 352, 39
 Zwaan M. A., Briggs F. H., Sprayberry D., Sorar E., 1997, ApJ , 490, 173
 Zwaan M. A., Meyer M. J., Staveley-Smith L., Webster R. L., 2005, MNRAS , 359, L30
 Zwaan M. A. et al., 2003, AJ , 125, 2842

Table A1. Schechter parameters for four sub-samples divided according to their local density derived by the classic version of the k -th nearest neighbour algorithm.

Region	α	log(M_{HI}^*/M_{\odot})
Least dense	-1.35 ± 0.08	9.86 ± 0.07
Second least dense	-1.30 ± 0.19	9.95 ± 0.16
Second most dense	-1.22 ± 0.12	9.89 ± 0.07
Most dense	-1.00 ± 0.25	9.82 ± 0.12

APPENDIX A: APPLYING THE CLASSIC K -TH NEAREST NEIGHBOUR METHOD

There is a strong argument for applying the HIPASS method of defining the local density on the HIZOA data to apply a direct comparison. In this appendix, we used the classic k -th nearest neighbour algorithm that was used by Zwaan et al. (2005) to define the environment. We divided our sample into four sub-samples and derived low-mass slope and characteristic mass for each sub-sample. Figure A1 shows the HIMF for these four sub-samples ranging from least dense environment (top-panel) to most dense environment (bottom-panel).

Table A1 presents the derived Schechter parameters for these four sub-sample ranging from low to high-density environment.

The exact same trend for the low mass slope α that is found when using the Bayesian k nearest neighbours analysis is also found when using the classic k -th nearest neighbour.

APPENDIX B: CORRECTION OF THE BAYESIAN K NEAREST NEIGHBOURS Σ_6

Because HIZOA is a flux-limited sample, the number of galaxies eventually starts dropping as a function of redshift. This implies that galaxies will appear increasingly isolated at larger redshift. If this is not taken into account, different density samples could mistakenly represent different distance ranges.

Whereas previous authors (Zwaan et al. 2005) have fit the data to correct for this bias, we chose a more robust correction based on the $S^3 - SAX$ semi-analytic simulation (Obreschkow et al. 2009). This simulation is based, in turn, on the the Millennium simulation of cosmic structure (Springel et al. 2005). Two samples have been selected: (A) a volume limited sample with $\log(M_{HI}^*/M_{\odot}) > 8.0$ and $v_{hel} < 12000 \text{ km s}^{-1}$; (B) a flux-limited sample with the same

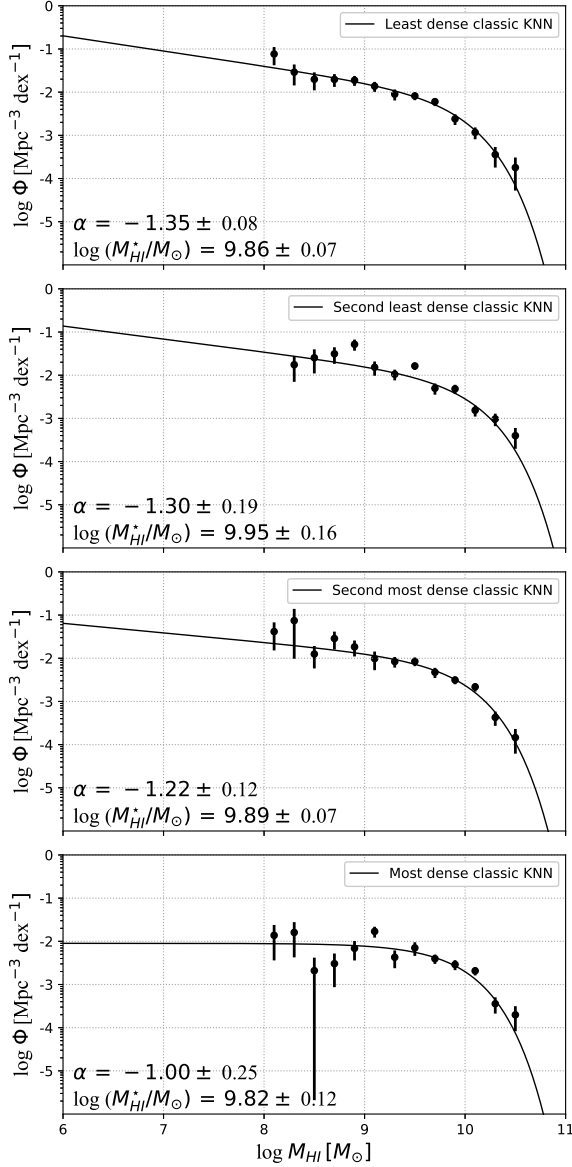


Figure A1. Four HIZOA HI mass function derived via the 2DSWML method based on the classic density estimation used in HIPASS. For comparison, the HIMFs are offset vertically to the normalization of the whole sample HIMF in Fig. 2.

hybrid-limit as HIZOA sample and $v_{\text{hel}} < 12000 \text{ km s}^{-1}$. For each sample, we used the same Bayesian k nearest neighbours algorithm to calculate the sixth nearest neighbour density, Σ_6 . We will refer to the sixth nearest neighbour density derived from the volume-limited sample as real, Σ_6^{real} , while for the flux-limited sample we will call it measured, $\Sigma_6^{\text{measured}}$.

Figure B1 shows the distribution of Σ_6^{real} as a function of redshift. As expected, for a volume-limited sample there is no obvious trend of Σ_6^{real} with redshift. We highlighted the flux-limited sample by the red dots.

On the contrary, Fig. B2 shows the distribution of $\Sigma_6^{\text{measured}}$ as a function of redshift. The same trend of decreasing $\Sigma_6^{\text{measured}}$ with redshift is seen as in the HIZOA sample in the top-panel of Fig. 3.

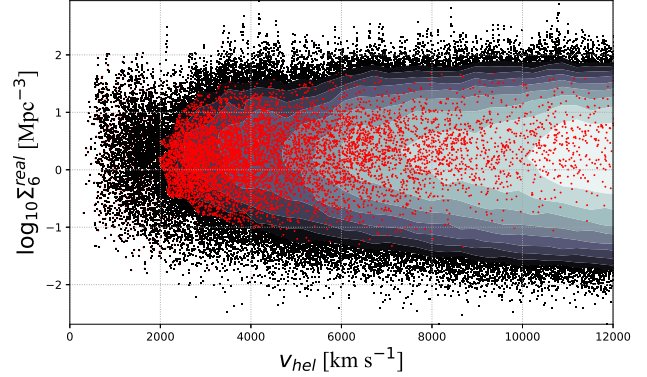


Figure B1. Scatter plot of the sixth nearest neighbour density, Σ_6 , with contours over-dense regions using the Bayesian k nearest neighbours algorithm for a volume-limited sample derived from the $S^3 - \text{SAX}$ simulation. The red dots highlight the flux-limited sample also derived from the $S^3 - \text{SAX}$ simulation.

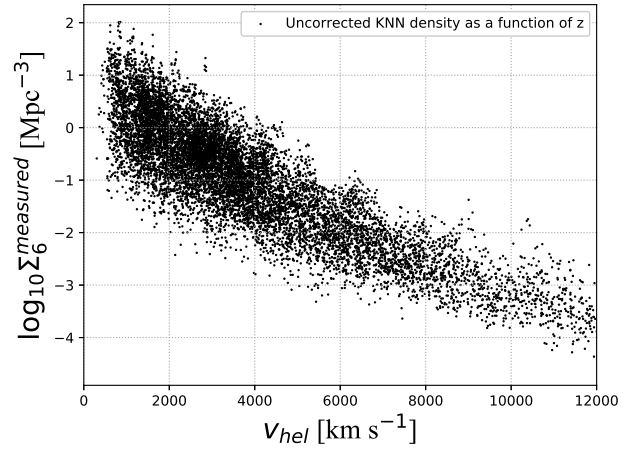


Figure B2. Scatter plot of the sixth nearest neighbour density, Σ_6 , using the Bayesian k nearest neighbours algorithm for a flux-limited sample derived from the $S^3 - \text{SAX}$ simulation.

To extract the exact trend that we should use to correct for our sample, we calculate the log of the ratio, $\Sigma_6^{\text{measured}}/\Sigma_6^{\text{real}}$, and plot the distribution in Fig. B3.

We fit a power-law to the mean and rms of the log of the ratio ($\Sigma_6^{\text{measured}}/\Sigma_6^{\text{real}}$) in 1000 km/s bins. We then subtract this derived power-law from the HIZOA $\Sigma_6^{\text{measured}}$ in the top-panel of Fig. 3 to obtain the corrected $\Sigma_6^{\text{corrected}}$ shown in the bottom-panel of Fig. 3.

The exact same method has been applied to correct the classic k -th nearest neighbour density but calculating classic Σ_6 for both volume- and flux-limited samples.

This paper has been typeset from a \LaTeX file prepared by the author.

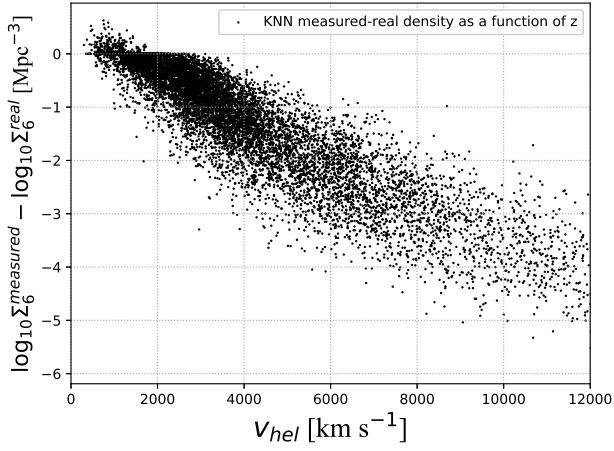


Figure B3. Scatter plot of the log of the ratio measured/real density as a function of redshift for a flux-limited sample derived from the $S^3 - SAX$ simulation.

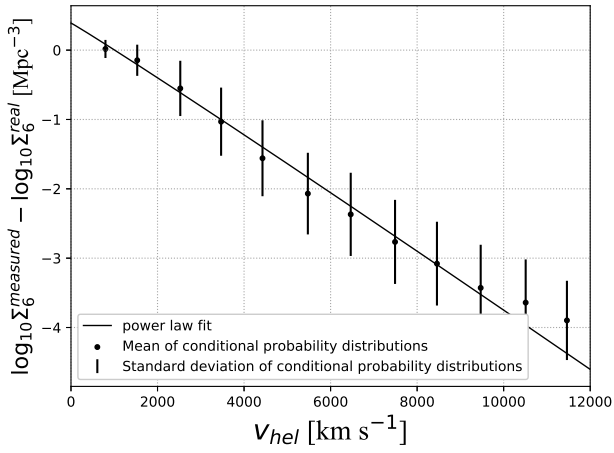


Figure B4. Mean and standard deviation of the conditional probability distribution of the ratio measured/real density as a function of redshift for a flux-limited sample. The solid line presents the power-law fit tot the conditional probability distribution.